Additive Manufacturing 111 (2025) 104969

Contents lists available at ScienceDirect

Additive Manufacturing

journal homepage: www.elsevier.com/locate/addma

Room-temperature laser crystallization of oxygen vacancy-engineered zirconia for additive manufacturing

Jaime A. Benavides-Guerrero [a], Luis F. Gerlein [a], Astrid C. Angel-Ospina [a], Paul Fourmont [a,b], Abhiroop Bhattacharya [a], Abbas Zirakjou [a], Fabrice Vaussenat [a], Caroline A. Ross [b], Sylvain G. Cloutier [a,*]

[a] Department of Electrical Engineering, École de Technologie Supérieure, 1100 Notre-Dame West, Montreal, QC, H3C 1K3 Canada
[b] Department of Materials Science and Engineering, Massachusetts Institute of Technology, 77 Massachusetts Ave., Cambridge, MA 02139, United States

ARTICLE INFO

Keywords:
Oxygen vacancies
Black-ZrO_2
Kinetics reaction
Laser crystallization

ABSTRACT

We demonstrate how strategically engineered oxygen vacancies enable room-temperature laser crystallization of zirconia (ZrO_2) in ambient air. Our sol-gel chelation synthesis creates amorphous ZrO_2 nanoparticles with a high concentration of oxygen vacancies that fundamentally alter the material's energy landscape. These defects create sub-bandgap states that facilitate visible light absorption and dramatically reduce the energy barrier for crystallization. Under low-energy laser irradiation (405–532 nm), oxygen vacancies mediate a rapid phase transformation mechanism where atmospheric oxygen interacts with vacancy sites, triggering ionic rearrangement and crystallization without conventional high-temperature processing. For comparison purposes, this study also explores the thermal crystallization of black zirconia in an oxidative atmosphere, a process typically performed under vacuum or inert conditions. Through comprehensive characterization (FTIR, EPR, XPS, XRD, Raman), we establish that vacancy-mediated crystallization produces monoclinic ZrO_2 with preserved defect structures, yielding a distinctive black phase with 25.6 % oxygen vacancy concentration, significantly higher than thermally processed counterparts (9.2 %). This vacancy-enabled crystallization circumvents the need for extreme temperatures (>1170°C) typically required for ZrO_2 processing, making it compatible with additive manufacturing. Using a modified 3D printer with a 405 nm laser, we demonstrate patterned crystallization of complex architectures, opening new possibilities for fabricating advanced ZrO_2-based devices for photocatalysis, fuel cells, and energy applications. This work provides fundamental insights into defect-mediated phase transformations and establishes a new paradigm for room-temperature ceramic processing.

1. Introduction

Advanced semiconducting ceramic materials are essential for numerous critical applications, including varistors [1], capacitors [2], piezoelectric devices [3], gas sensors [4], and solid oxide fuel cells [5]. While additive manufacturing offers promising avenues for fabricating complex ceramic architectures, crystallization processes vary significantly by material, from ~500°C for some bioceramics to > 1700°C for technical ceramics like alumina. For zirconia specifically, conventional crystallization to the monoclinic phase requires temperatures exceeding 1100°C, with phase transitions occurring at 1170°C (monoclinic to tetragonal) and 2370°C (tetragonal to cubic) [6,7]. These high temperatures limit compatibility with temperature-sensitive substrates and complicate ambient processing conditions.

Recent advances in laser-based characterization and processing have enabled unprecedented control over material phase and properties [8, 9]. In additive manufacturing, developments in wire-based friction stir [10], binder jetting [11], and laser-induced forward transfer [12] demonstrate the growing importance of room-temperature processing methods. For ceramic materials specifically, understanding phase transformation mechanisms at the atomic scale, including dislocation motion and defect interactions [13], is crucial for developing new processing strategies. The integration of laser processing with additive manufacturing [14] presents unique opportunities for fabricating functional ceramic components, provided that crystallization can be achieved without extreme temperatures.

* Corresponding author.
E-mail address: sylvaing.cloutier@etsmtl.ca (S.G. Cloutier).

https://doi.org/10.1016/j.addma.2025.104969
Received 3 July 2025; Received in revised form 2 September 2025; Accepted 15 September 2025
Available online 17 September 2025

Although laser-fabricated crystallized ceramics have been reported [15–17], these approaches generally rely on high-energy lasers and often focus on surface modification rather than defect-mediated transformations. Our work introduces a fundamentally different approach that leverages oxygen vacancies to facilitate room-temperature crystallization under low-energy laser irradiation.

Zirconia (ZrO_2) presents a compelling case for investigating defect-mediated property modifications. Pristine ZrO_2 is inherently non-reducible due to its high ionicity and wide band gap (3.2–5.09 eV) [18,19]. However, at the nanoscale, its electronic structure becomes amenable to modification through surface engineering [20]. Specifically, oxygen vacancies, which create in-gap energy states near the conduction band minimum [21,22], in contrast to cation vacancies that form levels above the valence band maxima [23], can dramatically transform ZrO_2's properties. High oxygen vacancy concentrations can narrow the band gap from 5.09 eV in white ZrO_2 to 1.52 eV in black ZrO_2 [24,25], enabling visible light absorption and potentially facilitating lower-energy crystallization pathways [26].

The monoclinic phase of ZrO_2 represents the thermodynamically stable polymorph at room temperature and atmospheric pressure, making it the target phase for applications requiring long-term structural stability [27,28]. While tetragonal and cubic phases require stabilization through doping or high temperatures (>1170°C for tetragonal, >2370°C for cubic), the monoclinic phase offers inherent stability combined with excellent chemical resistance and mechanical properties essential for catalytic and energy applications [5,29]. Recent advances in laser-based material processing have demonstrated the potential for controlled phase selection in ceramic materials [30,31], while developments in additive manufacturing highlight the need for room-temperature processing methods compatible with complex geometries and temperature-sensitive substrates [32,33]. However, conventional routes to crystalline monoclinic ZrO_2 require sintering temperatures exceeding 1100°C, incompatible with these emerging manufacturing paradigms [34].

The strategic integration of oxygen vacancies in ZrO_2 offers multifaceted advantages beyond facilitating low-temperature processing. These defects create charged surface states [35–37] that expand ZrO_2's application landscape to include cancer treatment [38], electrochemical sensing [39], biosensing [40], photocatalysis [41], photo-electrochemical solar cells [20], and even ferromagnetic materials [42]. However, conventional methods for synthesizing oxygen vacancy-rich ZrO_2 including high-temperature evacuation [43], high-pressure H_2 treatment [44], Ar^+ bombardment [45], molten lithium reduction [46], and high-pressure torsion [18] are energy-intensive and often yield suboptimal vacancy concentrations and distributions.

Sol-gel chemistry represents a particularly promising approach for oxygen vacancy engineering in zirconia. While traditional sol-gel synthesis is well-established for ZrO_2 [47–50], its potential for controlled introduction of oxygen vacancies has been underexplored. Most current sol-gel methods yield low oxygen vacancy concentrations, necessitating high-temperature post-treatments in reducing atmospheres to enhance vacancy formation [51]. Similarly, doping sol-gel-derived ZrO_2 with metallic nanoparticles can generate oxygen vacancies but still requires high-temperature processing [52,53]. Recent studies by Imparato et al. [54] have shown that introducing complexing agents followed by thermal treatment at 400°C can create visible light-responsive ZrO_2, suggesting the feasibility of defect engineering through sol-gel chemistry.

The novelty of our approach lies in the strategic modification of sol-gel chemistry to directly produce high-quality amorphous oxygen vacancy-rich ZrO_2 without post-treatments. Building upon our previous work with titania [55], we have developed a chelation-controlled sol-gel method that precisely regulates the hydrolysis and condensation rates of zirconium precursors. By employing acetylacetone as a chelating agent and implementing extended aging, we achieve unprecedented control over oxygen vacancy formation at the nanoparticle surface. Unlike conventional sol-gel methods that create uniform ZrO_2, our approach deliberately engineers structural defects that fundamentally alter the material's energy landscape.

This work demonstrates how these strategically incorporated oxygen vacancies enable room-temperature laser-induced crystallization in ambient conditions, a significant departure from traditional thermal processing requirements. The amorphous oxygen vacancy-rich ZrO_2 nanoparticles exhibit enhanced visible light absorption, facilitating crystallization under low-energy laser irradiation without the need for vacuum environments or metallic dopants. Through comprehensive characterization using FTIR, EPR, UV-Vis, Raman spectroscopy, TEM, and XPS, we elucidate the role of oxygen vacancies in the laser-induced crystallization process and benchmark these materials against thermally crystallized counterparts. By enabling ambient laser patterning of complex ZrO_2 structures, this approach represents a significant advancement toward practical additive manufacturing of functional zirconia-based architectures.

2. Methods

2.1. Synthesis

The synthesis of the oxygen vacancy-rich red-ZrO_2 is done through sol-gel chemistry as shown in Fig. 1(a). The synthesis process involves the mixing of the solvent (ethanol) and the chelating agent (acetylacetone) with the zirconium precursor (Zirconium (IV) butoxide). The use of acac reduces the reactivity of the zirconium alkoxide toward water, effectively modulating hydrolysis kinetics and promoting the controlled generation of oxygen vacancies during aging. The detailed synthesis procedure is described in detail in the *Materials* section of this manuscript.

The chemical reactions can be controlled through the hydrolysis and complexation molar ratios [56]. We define these two ratios as r_w= [H_2O]/[Zr] and r_c= [acac]/[Zr], respectively. A precise control of these ratios yields cluster solutions, stable sols, transparent and opaque gels and precipitated powders. [57] The ratios that we use in this work are summarized in the Table 1.

To obtain red-ZrO_2 rich in oxygen vacancies, we must decrease the kinetics of the hydrolyzation reaction. To do so, we use $Zr(OBu)_4$ containing four (butoxy) carbon atoms in the organic chain. The length of the organic chain in metal alkoxides is known to be inversely proportional to its reactivity towards hydrolyzation in the sol-gel process [58]. Indeed, the reactivity of alkoxy groups towards hydrolysis decreases as the number of carbon atoms in the organic chain increases [57]. It is also common to dilute the precursor in alcohols or mix it with complexing agents to reduce its reactivity towards water [58]. In this study, we use acetylacetone (acac) as a complexing agent (r_c=0.65) to chelate the metallic cation on the $Zr(OBu)_4$ precursor and delay its hydrolyzation. The mechanism responsible for the reaction between acac and $Zr(OBu)_4$ can be explained by the following interexchange substitution reaction [58]:

$$Zr(OBu^n)_4 + acacH \rightarrow Zr(OBu^n)_{4-x}(acac)_x + xBuOH$$

Over an extended aging period of 8 months, we observe a gradual change in the color of the solution from light-yellow, to orange and to blood-red. This change in color is directly attributed to the formation of oxygen vacancies. It stems from the charge transfer from the complexing agent (acac) to the Zr^{4+} ion [59,60] and the formation of peroxo complexes that display an intense orange or red color in solution [58,61,62]. These peroxo complexes also enhance the visible light photoexcitation of semiconductor materials [63,64]. Finally, we obtain the red amorphous ZrO_2 rich in oxygen vacancies shown in Fig. 1(a) [59]. The extended duration, though a limitation for scalability, is necessary to achieve the exceptionally high oxygen vacancy concentration (>25 %)

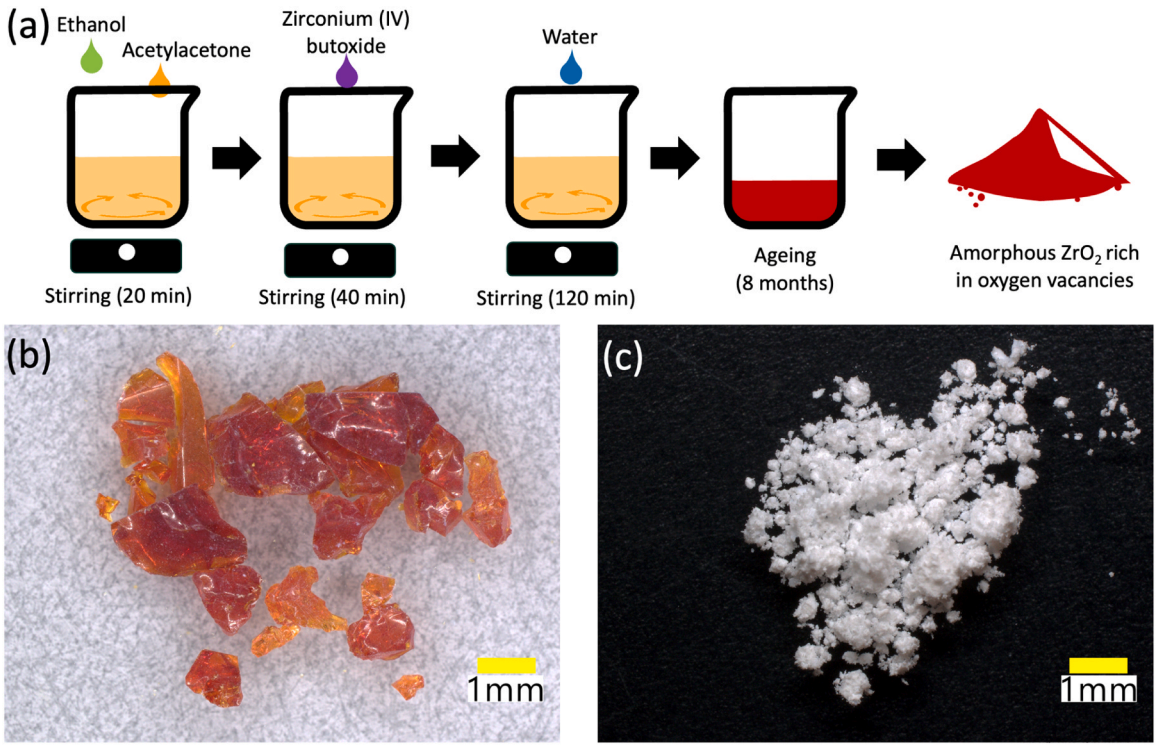

Fig. 1. (a) Amorphous red-ZrO_2 synthesized by sol-gel method. (b) Oxygen vacancy-rich red-ZrO_2. (c) Conventional oxygen vacancy-free white-ZrO_2.

Table 1
Hydrolysis and complexation ratios used for the synthesis of the conventional (white) and the oxygen vacancy-rich (red) ZrO_2 particles.

ZrO_2 powder	r_w= [H_2O]/[Zr]	r_c= [acac]/[Zr]
White ZrO_2 (Fig. 1a)	2.44	0
Red ZrO_2 (Fig. 1b)	2.44	0.65

validated by XPS and EPR analyses in later sections.

As a control experiment, we synthesize ZrO_2 without any complexing agent (rc = 0), through the standard hydrolysis and condensation of zirconium (IV) butoxide ($Zr(OBu)_4$) [65,66]. The hydrolysis reaction is exothermic and takes only few seconds to complete [52]. Afterwards, the condensation reaction takes place to yield amorphous ZrO_2 nanoparticles precipitating at the bottom of the beaker [65,66]. Although the whole process is completed in few seconds, the system is typically aged for 72 h before the solvent is evaporated and the usual white-colored amorphous ZrO_2 powder shown in Fig. 1(b) is obtained. [52] Due to the absence of chelating agents and slow hydrolysis control, this material lacks significant oxygen vacancy content and serves as a comparative material.

3. Results and discussion

3.1. Characterization of the amorphous red-ZrO_2 powder

3.1.1. Structural and chemical analysis

The formation of the $Zr(OBu)_4$-acac complex and the nature of the acac-Zr bond are probed by FTIR spectroscopy. Fig. 2(a) shows the comparative FTIR spectra of the oxygen vacancy-rich (red) ZrO_2 powder versus the conventional (white) ZrO_2.

In the red ZrO_2 sample, we identified characteristic bands at 1524 cm^{-1} (γC=O) and 1423 cm^{-1} (νC=C) [67], confirming the presence of acetylacetonato groups in the enol form coordinated to zirconium atoms. The band at 1278 cm^{-1} corresponds to νC-CH_3 group bonded to the acac [68] suggesting the complete reaction of the acac with the Zr cation [68,69]. The absence of the characteristic acac band at 1620 cm^{-1} supports this conclusion. As expected, these bands are negligible in the white ZrO_2 spectrum, indicating no acac-Zr interaction (rc = 0). The band at 1365 cm^{-1}, common to both spectra, is directly attributed to the δCH_3 groups from $Zr(OBu)_4$, acac and the solvent [68,70].

Based on FTIR analysis and supported by previous studies [71,72], we propose a symmetric trimer structure for the $Zr(OBu)_4$-acac complex (Fig. 2(b)), where two or three acac ligands coordinate to each surface zirconium atom. This complex formation inhibits condensation and polymerization reactions of $Zr(OBu)_4$, resulting in the formation of red amorphous ZrO_2 with controlled oxygen deficiency [71,73].

3.1.2. Characterization of oxygen vacancies

We employed multiple complementary techniques to characterize and quantify oxygen vacancies in our materials:

Electron Paramagnetic Resonance (EPR): Fig. 2(c) shows electron paramagnetic resonance (EPR) spectra of the amorphous red-ZrO_2 powder. EPR is a common method to probe paramagnetic materials and identify Zr^{3+} species, oxygen vacancies and the electrons produced by the desorption of lattice oxygen ions that reduce Zr^{4+} ions to Zr^{3+} ions [74,75]. EPR is highly sensitive, capable of detecting unpaired electrons at concentrations as low as parts per billion [76]. The observed signals with g-values between 2.003 and 2.006 are attributed to superoxide anion radicals coordinated to surface Zr^{4+} ions [77], and to unpaired electrons associated with oxygen vacancies and reduced Zr centers [78,79].

UV-Visible Spectroscopy: Fig. 2(d) displays UV–visible absorption spectra of the amorphous red-ZrO_2, revealing a broad absorption band from 340 nm to 600 nm. This unusual visible light absorption in ZrO_2 (which typically absorbs only in the UV region) is directly correlated with oxygen vacancy concentration and the presence of Zr^{3+} ions [80].

Band Structure Modification and Crystallization Mechanism: As illustrated in Fig. 2(e), oxygen vacancies create intermediate states within the ZrO_2 bandgap that are crucial for the laser-induced crystallization mechanism. These states enable efficient visible light absorption

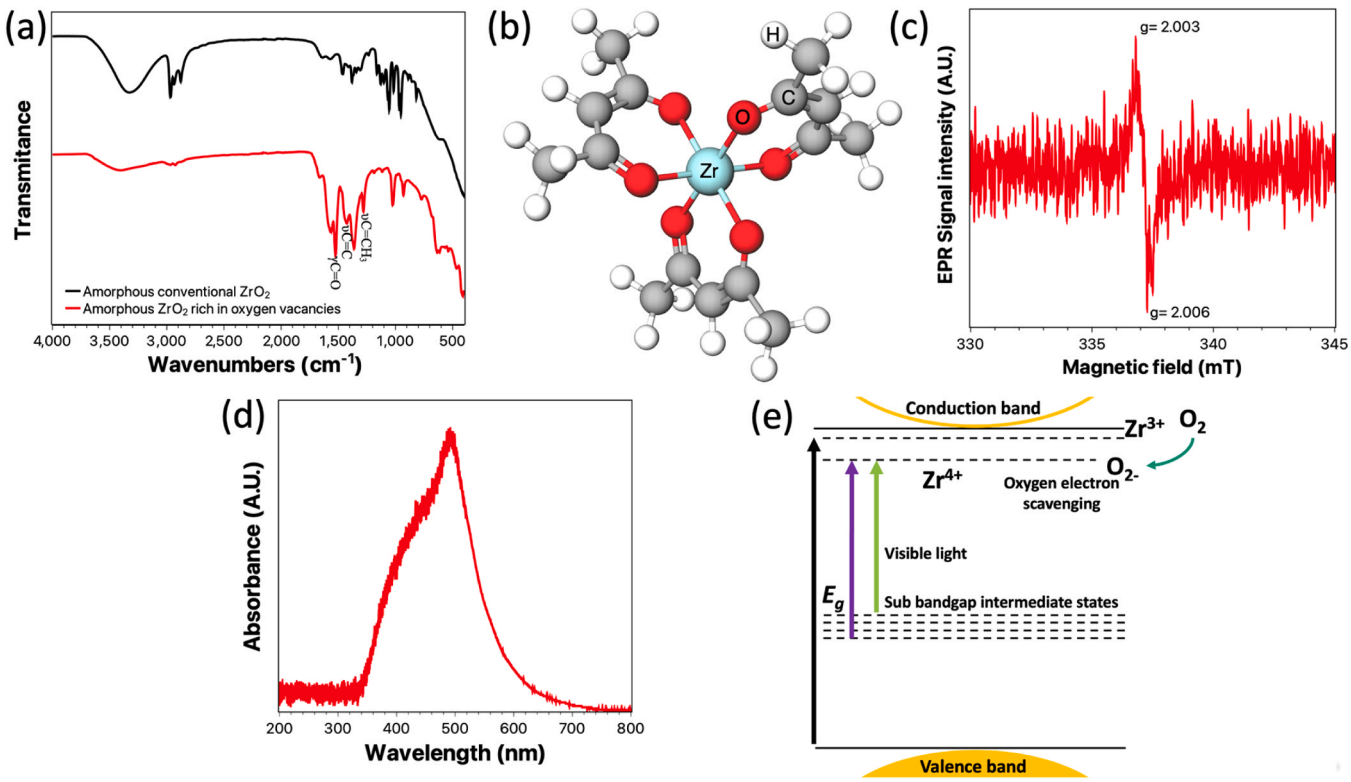

Fig. 2. Characterization of the amorphous red-ZrO_2 powder rich in oxygen vacancies. (a) Comparison of the FTIR absorption spectra for the red-ZrO_2 powder and conventional vacancy-free white-ZrO_2 powder. (b) Schematic representation of the $Zr(OBu)_4$ molecule chelated by acac during the synthesis. (c) EPR spectrum of the amorphous red-ZrO_2 powder. (d) UV–vis spectra of the amorphous red-ZrO_2 powder. (e) Schematic representation of the energy diagram with sub-bandgap states created by the oxygen vacancies. The proposed reaction for the laser-assisted phase transition process is also illustrated.

while increasing the material's Urbach energy [81]. Importantly, the red amorphous ZrO_2 already possesses oxygen vacancies from our chelation-controlled sol-gel synthesis (Fig. 2c), the laser irradiation does not create additional vacancies but rather triggers crystallization while preserving them. The mechanism proceeds through sequential steps: (1) absorption of 405–532 nm photons via vacancy-induced sub-bandgap states, (2) excitation of electrons to the conduction band, (3) interaction with atmospheric oxygen molecules that act as effective photo-excited electron scavengers [82,83], (4) adsorption of O_2 molecules on the red ZrO_2 nanoparticle surface to partially compensate for the oxygen vacancies [84], and (5) enhanced ionic mobility induced by oxygen vacancies that facilitates the amorphous-to-monoclinic phase transformation [82]. The presence of oxygen vacancies promotes the formation of Zr^{3+} sites by distributing the electrons left behind by the vacancy to contiguous Zr sites, thereby reducing them from Zr^{4+} to Zr^{3+} [84].

3.2. Laser-induced crystallization of oxygen-deficient ZrO_2

3.2.1. Real-time phase transformation monitoring

To demonstrate and characterize the phase transformation from amorphous red-ZrO_2 to crystalline black-ZrO_2, we performed in-situ monitoring using Raman micro-spectroscopy (Witec alpha300 system with 0.5 cm^{-1} spectral resolution). Fig. 3(a) shows the evolution of Raman spectra over a 100-second interval following laser irradiation with a continuous-wave 532 nm laser at a power density of 270 W/mm^2. The crystallization process occurred rapidly, with characteristic monoclinic ZrO_2 peaks developing within seconds of irradiation.

Fig. 3(b) quantifies this transformation, showing that maximum intensity for the characteristic monoclinic phase peaks at 175 and 185 cm^{-1} was reached after approximately 30 s of irradiation. This rapid crystallization at room temperature and low laser power (compared to

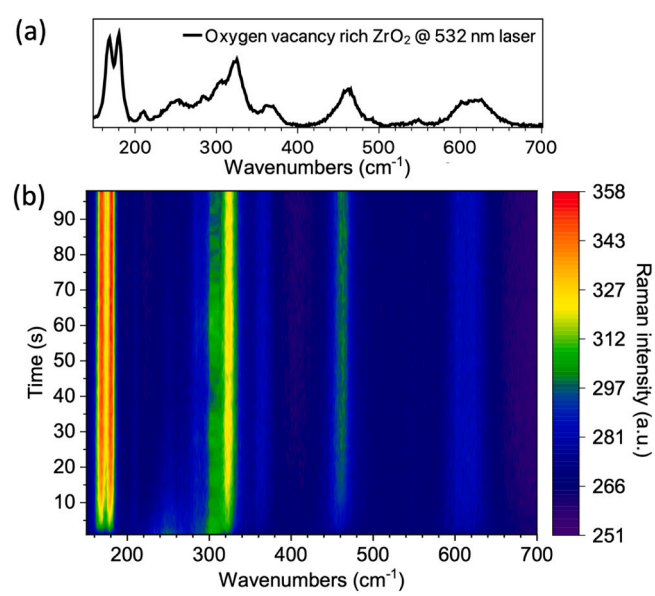

Fig. 3. (a) Raman micro-spectroscopy result for the crystallized (red) amorphous ZrO_2. (b) Transient evolution of the laser-assisted crystallization process.

conventional sintering temperatures of >1100°C) demonstrates the effectiveness of our oxygen vacancy engineering approach.

Raman spectroscopy is also a suitable technique to investigate the oxygen vacancies from the red-ZrO_2 powder, as it can detect the disorder in the first atomic layers and the lattice defects that are not visible by XRD [41,85]. The Raman spectra recorded during the laser-crystallization show the main characteristic peaks of the

monoclinic ZrO_2 (m-ZrO_2), with a slight broadening and blue shift. This peak position dependence on the oxygen content is well documented [86] and directly attributed to the presence of oxygen vacancies [41]. The mechanism involves the disruption of the crystal structure of the surface Zr-O units due to oxygen vacancies, which leads to the disordered surface [41]. Most importantly, the Raman analysis suggests that this oxygen vacancy-rich red-ZrO_2 crystallized by laser reaches a higher degree of crystallization than the crystallized ZrO_2 obtained using thermal conversion of other oxygen vacancy-rich powders [41].

While no external heating is applied, the absorbed laser energy (270 W/mm^2 at 532 nm or 240 W/mm^2 at 405 nm shown later in this document) does cause localized temperature increases. Based on similar laser processing studies [31,87], we estimate local temperatures of 200°C at the irradiation spot. To quantify these effects, we monitored the laser crystallization process using a thermal imaging system (FLIR ETS320) with emissivity set to 0.8 [88]. The maximum recorded temperature was 193°C at the laser focal point, with rapid spatial decay maintaining the surrounding material below 50°C (Figure S6), still significantly below the 1170°C required for conventional thermal crystallization.

The rapid thermal dissipation prevents bulk heating, maintaining the substrate at near-ambient temperature. This localized, transient heating combined with the photon-assisted vacancy mechanism enables crystallization without the sustained high temperatures that would annihilate oxygen vacancies [89]. This localized heating, combined with the photon-assisted vacancy mechanism, drives the amorphous-to-crystalline transformation without grain coarsening, as evidenced by the ~20 nm crystallite size (Fig. 4).

3.2.2. Structural confirmation of laser-crystallized ZrO_2

Transmission electron microscopy (TEM) was employed to validate the crystalline phase of laser-crystallized ZrO_2. Fig. 4 presents TEM micrographs showing well-defined crystalline structures. The average particle size (Fig. 4(a)) is approximately 20 nm, with a relatively narrow size distribution. High-resolution imaging (Fig. 4(b)) reveals clear lattice fringes, confirming successful crystallization.

Selected area electron diffraction (SAED), shown in the inset of Fig. 4 (b), displays well-defined diffraction rings corresponding to the (111), (200), and (211) planes of monoclinic ZrO_2. The measured interplanar distance of 0.31 nm matches the expected d-spacing for the (111) plane of monoclinic ZrO_2 [90].

3.3. Thermal crystallization of oxygen-deficient ZrO_2

3.3.1. Comparative analysis of thermal vs. laser crystallization

Prior to treatment, the standard white-ZrO_2 and the oxygen-deficient red-ZrO_2 powders remains fully amorphous, as evidenced by FTIR spectroscopy showing only organic ligand signatures (Fig. 2a).

To establish a comparative baseline, we performed conventional thermal annealing of both standard white-ZrO_2 and oxygen-deficient red-ZrO_2 at 1170°C in air. The standard white-ZrO_2 powder was annealed for 60 min, while the oxygen-deficient red-ZrO_2 was annealed for only 60 s to minimize oxygen vacancy loss through diffusion (which becomes significant above 450°C) [89].

As shown in Fig. 5(a), the standard white-ZrO_2 powder retained its white color after thermal crystallization, while Fig. 5(b) demonstrates that oxygen-deficient red-ZrO_2 transformed to black-ZrO_2 after just 60 s of thermal treatment. Upon thermal treatment, both materials undergo phase transformation to monoclinic structure, confirmed by TEM analysis (Figure S1, Supplementary Information) and XRD (Figure S2, Supplementary Information), but with markedly different characteristics. The black ZrO_2 (from red precursor) exhibits broader XRD peaks and matches with oxygen-deficient reference patterns ($O_{0.66}Zr_3$, 00–021–1498), while white ZrO_2 shows sharp peaks consistent with stoichiometric baddeleyite (00–013–0307). This color change from red to black is consistent with structural rearrangements of Zr-O units on the nanoparticle surface caused by the presence of oxygen vacancies [41,59, 91], confirming that the transformation represents a phase change from amorphous to oxygen-deficient monoclinic structure while preserving the vacancy concentration during crystallization.

3.3.2. Spectroscopic comparison of crystallization methods

Fig. 5(c) compares Raman spectra for standard white m-ZrO_2 (thermally crystallized), black m-ZrO_2 (thermally crystallized), and black m-ZrO_2 (laser crystallized). All three samples exhibit characteristic peaks of monoclinic ZrO_2, confirming successful phase transformation regardless of processing method [92].

The standard white m-ZrO_2 shows expected monoclinic features at 178, 191, 223 (Bg), 308 (Bg), 334 (Bg), 345 (Ag), 382 (Ag), 477 (Ag), 503 (Bg), 537 (Bg), 558 (Ag), 573, 614 (Bg), and 638 cm^{-1} (Ag) [85,93, 94]. In contrast, both black m-ZrO_2 samples (thermally and laser crystallized) show peaks at 175, 185, 216 (Bg), 308 (Bg), 329 (Bg), 372 (Ag), 467 (Ag), 550 (Ag), 573, 607 (Bg), and 629 cm^{-1} (Ag) that are broader and shifted to lower frequencies.

These spectral differences provide clear evidence for the presence of

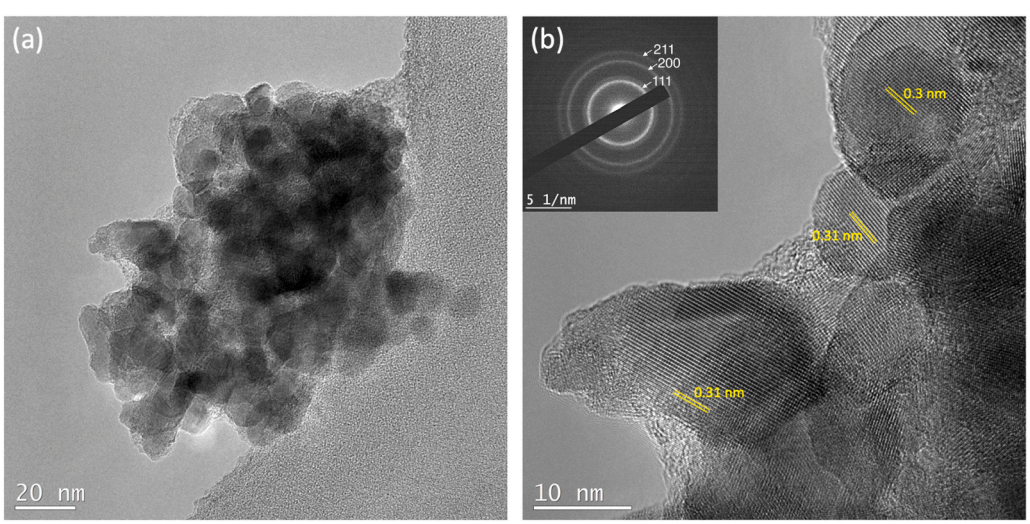

Fig. 4. TEM characterization of the oxygen vacancy-rich ZrO_2 nanoparticles after laser-induced crystallization. (a) Powder morphology observed at low resolution. (b) Lattice fringes visible at higher resolution. The inset shows the SAED pattern.

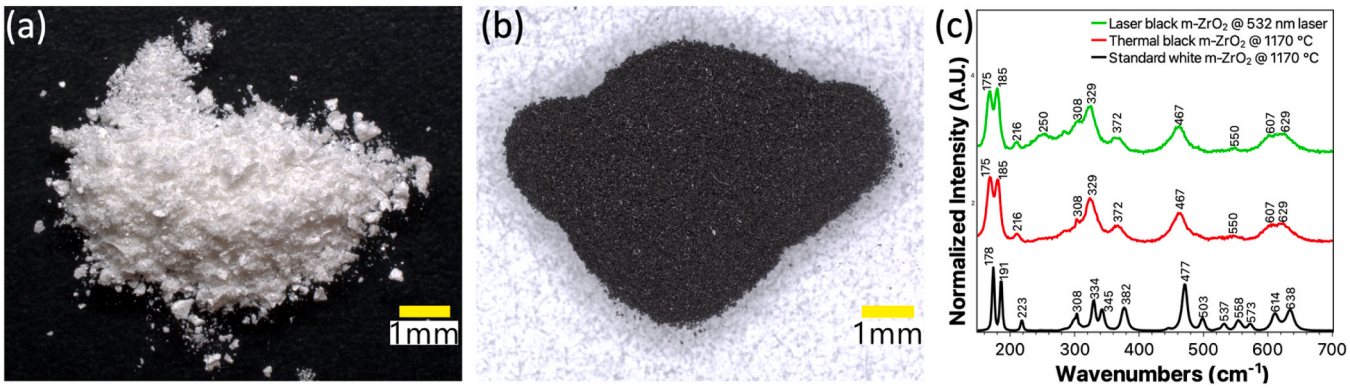

Fig. 5. Crystalline ZrO_2 nanoparticles after thermal annealing at 1170 °C. (a) Thermally crystallized standard white m-ZrO_2 powder. (b) Thermally crystallized black m-ZrO_2 powder. (c) Raman micro-spectroscopy results for the standard white m-ZrO_2 powder (thermally-converted at 1170 °C), black m-ZrO_2 (thermally-converted at 1170 °C) and black m-ZrO_2 (laser-converted at 532 nm and 270 W/mm [2]).

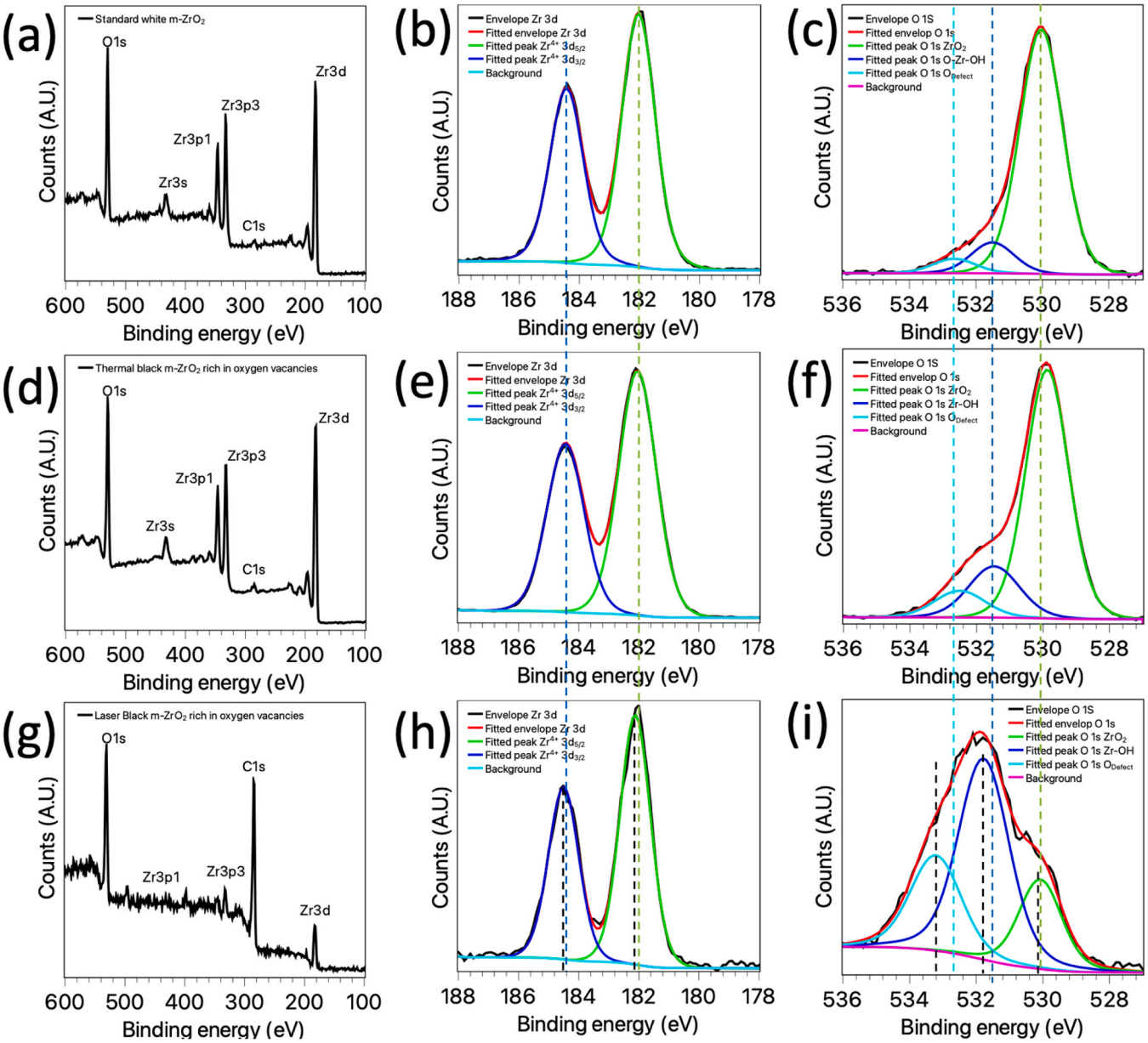

Fig. 6. X-ray photoelectron spectroscopy (XPS) for the thermal crystallized standard monoclinic ZrO_2 ((a), (b), (c)), thermal crystallized monoclinic black ZrO_2 ((d), (e), (f)) and the laser crystallized monoclinic black ZrO_2 ((g), (h), (i)).

oxygen vacancies in both black m-ZrO_2 samples, as such defects alter the local symmetry and vibrational modes of the ZrO_2 lattice [85]. A distinct peak at 250 cm^{-1} appears exclusively in the laser-crystallized sample, which has been specifically attributed to oxygen vacancies and vibrational modes of the oxygen sublattice in a disordered state [85,95].

3.4. Quantitative analysis of oxygen vacancies in crystalline ZrO_2

3.4.1. X-ray photoelectron spectroscopy analysis

X-ray photoelectron spectroscopy (XPS) was employed to quantitatively assess oxygen vacancy concentrations and electronic structure differences among the samples. Fig. 6 presents the survey scans and high-resolution spectra of the Zr3d and O1s regions for standard white m-ZrO_2, thermally crystallized black m-ZrO_2, and laser crystallized black m-ZrO_2.

The carbon peaks observed in all survey scans (Fig. 6(a), (d), and (g)) are attributed to residual carbon from the $Zr(OBu)_4$ precursor used in the sol-gel synthesis [96,97]. These peaks are most pronounced in the laser-crystallized sample, as laser treatment only crystallizes the surface while leaving underlying amorphous material with higher carbon content.

In the Zr3d region, peaks at approximately 182.2 eV ($Zr3d_{5/2}$) and 184.4 eV ($Zr3d_{3/2}$) correspond to Zr in ZrO_2 [97–101]. Comparing Fig. 6 (b), (e), and (h), we observe a slight shift (0.2–0.4 eV) toward higher binding energies in the laser-crystallized sample compared to standard white m-ZrO_2 and thermally crystallized black m-ZrO_2.

This shift appears counterintuitive, as oxygen vacancies typically create electronic states near the conduction band in most metal oxides, leading to lower binding energies [98]. However, ZrO_2 exhibits distinctive behavior: oxygen vacancy states are located closer to the middle of the bandgap, significantly farther from the conduction band. Consequently, electrons in these vacancy states have limited mobility toward the conduction band, resulting in positively charged vacancies that cause downward band bending and a shift toward higher binding energies in XPS [102].

Analysis of the O1s region reveals peaks at ~530–530.7 eV attributed to Zr-O bonds [26], while peaks between ~531.5–532.7 eV correspond to oxygen ions in surface vacancy sites (O_{defect}) and chemisorbed oxygen species (e.g., OH^-) [103]. The peak at 533.2 eV, indicative of oxygen vacancies, shows significantly higher intensity in the laser-crystallized sample (Fig. 6(i)) compared to the standard white m-ZrO_2 (Fig. 6(c)) [26].

Through quantitative analysis of O1s peak areas [26] (see Table S1, Supplementary Information), we determined relative oxygen vacancy concentrations of 9.2 % for thermally crystallized black m-ZrO_2 and 25.6 % for laser-crystallized black m-ZrO_2. This substantial difference demonstrates the superior preservation of oxygen vacancies during room-temperature laser processing compared to high-temperature thermal treatment.

3.4.2. Electron paramagnetic resonance comparison

Fig. 7 presents EPR spectra comparing the three crystallized ZrO_2 samples. Both black m-ZrO_2 samples exhibit signals with g-values between 2.000 and 2.003, attributed to electron trapping at oxygen vacancies [24,78,79,104]. The signal at g = 2.0023, present in both black m-ZrO_2 samples but absent in standard white m-ZrO_2, is specifically associated with Zr^{3+} paramagnetic centers linked to line defects or grain boundaries. In ionic oxides such as ZrO_2, these defect sites are known to introduce energy levels high within the bandgap, as depicted in Fig. 2 (e), enabling electrons to be easily excited into the conduction band [104]. This observation aligns with the laser-assisted crystallization mechanism proposed for black m-ZrO_2, as illustrated in Fig. 3. Supporting this interpretation, the standard white m-ZrO_2 does not exhibit any of the aforementioned EPR signals, consistent with the absence of paramagnetic oxygen vacancies in the material.

The persistence of these EPR signals even after processing in an oxidative atmosphere (air) indicates a remarkable stability of oxygen vacancies in our materials. The higher signal intensity in the laser-crystallized sample compared to the thermally crystallized sample aligns with our XPS findings (Figs. 6(f) and 6(i)), confirming superior oxygen vacancy preservation during room-temperature laser processing. This difference can be attributed to the high-temperature conditions (1170°C) used for thermal crystallization, which promote outward diffusion of oxygen vacancies, a well-documented phenomenon that occurs above 450°C due to entropy-driven processes [89,105].

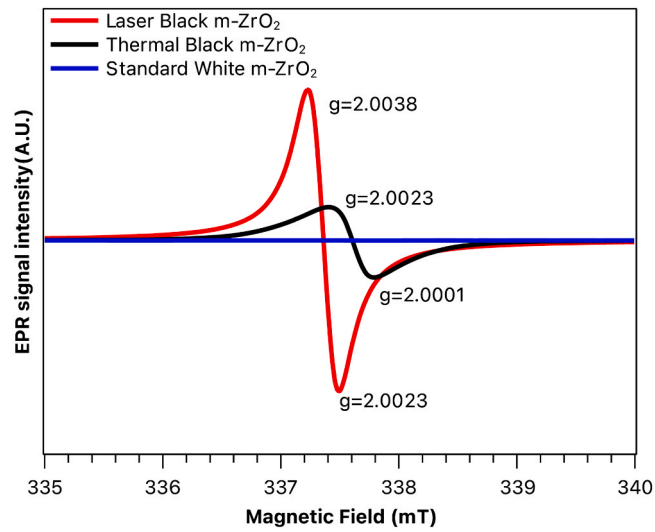

Fig. 7. Comparison of the EPR spectra of the thermally- and laser-crystallized m-ZrO_2 samples.

3.5. Laser patterning of complex structures using oxygen-deficient ZrO_2

3.5.1. Demonstration of patterning capabilities

To demonstrate the potential of our approach for additive manufacturing applications, we employed a standard commercial filament-based 3D printer equipped with a continuous-wave 405 nm laser printhead. This apparatus has been fully described in other works [31,55]. By applying a laser power density of 240 W/mm^2, we achieved controlled crystallization of amorphous red-ZrO_2 into black m-ZrO_2 with spatial precision, enabling the creation of complex patterns as shown in Fig. 8.

The selection of 405 nm laser wavelength was strategically based on the optical properties of our oxygen-deficient ZrO_2. UV–visible spectroscopy analysis (Fig. 2d) confirms strong absorption at this wavelength, which falls within the broad 340–600 nm absorption band created by oxygen vacancy-induced sub-bandgap states. This wavelength provides optimal coupling between the laser energy and the electronic transitions facilitated by the vacancy states (Fig. 2e), enabling efficient room-temperature crystallization. Additionally, 405 nm lasers are standard components in commercial 3D printing systems, ensuring practical implementation of our approach without requiring specialized equipment.

Fig. 8(a) presents a micrograph of a laser-crystallized pattern, where the darker laser-treated region is clearly delineated from the surrounding untreated material. Fig. 8(b) shows a high-resolution 3D topographic reconstruction obtained using laser scanning microscopy, demonstrating that the laser treatment achieves a penetration depth of up to 18 μm while maintaining pattern fidelity. The details of the procedure and the optimal processing parameters are provided in the supplementary section.

The selection of oxygen-deficient red ZrO_2 over conventional white ZrO_2 for additive manufacturing is critical to the success of this approach. While white ZrO_2 exhibits negligible visible light absorption

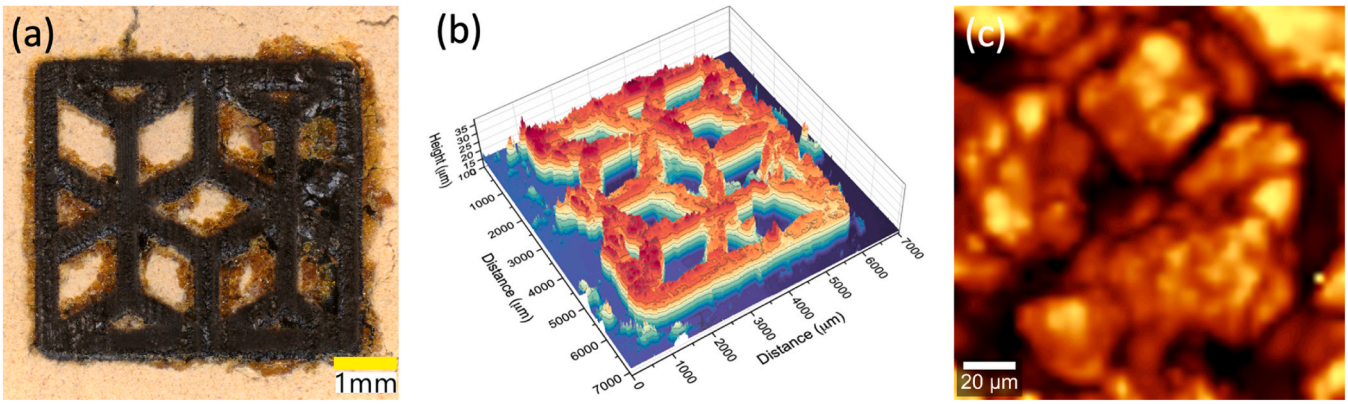

Fig. 8. Complex laser-crystallized ZrO_2 structure. (a) Microscopy image of the crystallized structure. (b) Typical topographic 3D surface reconstruction of the laser crystallized structure. (c) Micro-Raman image of the laser-crystallized surface. The image corresponds to the intensity of the 175 cm^{-1} and 185 cm^{-1}Raman peaks.

due to its wide bandgap (5.09 eV) and lack of oxygen vacancies, the red ZrO_2 demonstrates broad absorption from 340 to 600 nm (Fig. 2d) enabled by its 25.6 % oxygen vacancy concentration. This fundamental difference allows red ZrO_2 to undergo room-temperature crystallization under low-energy visible laser irradiation (240–270 W/mm^2), whereas white ZrO_2 would require conventional thermal processing exceeding 1170°C, conditions incompatible with 3D printing platforms and temperature-sensitive substrates. This vacancy-mediated visible light responsiveness represents the key innovation enabling direct laser writing of crystalline ZrO_2 architectures.

3.5.2. Structural integrity and phase confirmation

The monoclinic phase of the laser-crystallized structures was confirmed by Raman micro-spectroscopy (Figure S3, Supplementary Information). Fig. 8(c) presents an intensity Raman mapping of the characteristic monoclinic ZrO_2 peaks at 175 and 185 cm^{-1} , clearly delineating the patterned region.

The Raman mapping reveals microcracks in the laser-treated region, attributed to rapid densification during crystallization [87]. While these defects represent a limitation of the current process, ongoing optimization of laser parameters (power density, scan speed, and beam profile) aims to minimize crack formation while maintaining high oxygen vacancy concentration.

3.5.3. 3D additive manufacturing of crystalline ZrO_2

To demonstrate true 3D additive manufacturing capability, we fabricated multi-layered ZrO_2 structures using sequential powder deposition and laser crystallization. Two geometries were produced: a hollow square and a hollow cylinder, both reaching approximately 3 mm in height. The fabrication process involved manual deposition of

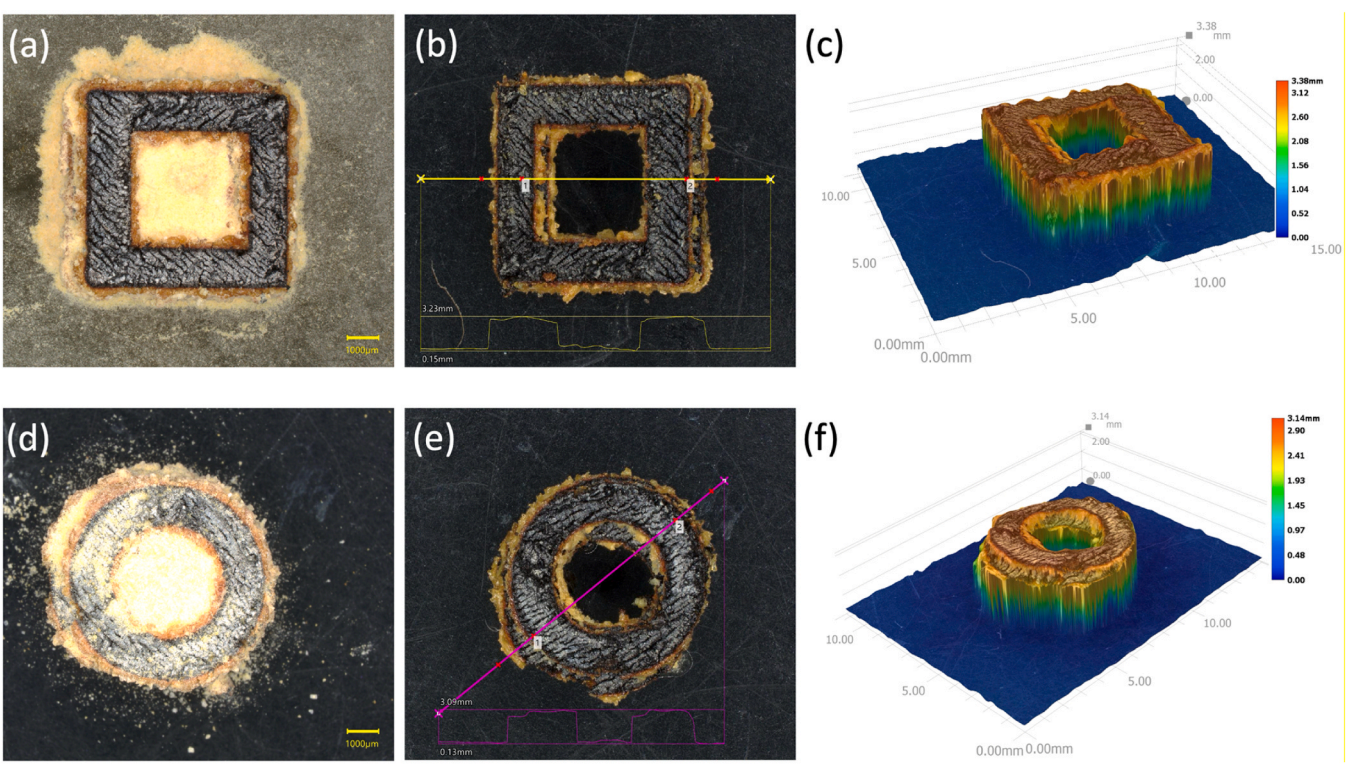

Fig. 9. 3D printed crystalline ZrO2 structures. (a–c) Hollow square: (a) before powder removal, (b) after isopropanol washing (wall width 3.23 mm, height 2.90 mm), (c) 3D topographic reconstruction. (d–f) Hollow cylinder: (d) with residual unconsolidated powder, (e) after washing (wall width 2.81 mm, height 3.00 mm), (f) 3D topographic reconstruction.

amorphous red-ZrO2 powder layers followed by selective laser crystallization (405 nm, 240 W/mm^2) of each layer before adding subsequent material. After completing the structures, unconsolidated powder was removed by washing with isopropanol, revealing the final crystallized geometries.

Fig. 9 presents the 3D structures fabricated through layer-by-layer deposition and laser crystallization. The hollow square structure (Fig. 9a-c) reached 2.90 mm in height, while the hollow cylindrical structure (Fig. 9d-f) achieved 3.00 mm. Cross-sectional height profiles demonstrate successful layer consolidation: the square structure shows consistent heights of 2.89 mm and 2.90 mm at two measurement points (Figure S4), while the cylinder exhibits heights of 2.81 mm and 3.00 mm (Figure S5). Although manual powder deposition introduced some lateral shifting between layers, the structures maintained integrity throughout the building process, confirming the viability of vacancy-mediated crystallization for multi-layer fabrication.

These proof-of-concept structures demonstrate several key achievements: (i) successful interlayer adhesion through vacancy-mediated crystallization without additional binders, (ii) preservation of structural integrity across multiple layers without delamination, and (iii) ability to create both solid walls and hollow geometries. The 18 μm laser penetration depth proved sufficient for layer consolidation while maintaining the black crystalline phase throughout the structure.

While manual powder deposition introduced some geometric irregularities, this limitation can be addressed through integration with automated powder-bed or dispensing systems available in commercial ceramic 3D printers. The successful fabrication of millimeter-scale structures validates the potential for scaling to larger components while maintaining the unique properties conferred by oxygen vacancies. Future optimization will focus on automated powder handling, layer thickness control (targeting 20–50 μm), and complex geometry fabrication for functional devices in photocatalysis and energy applications.

3.6. Phase transformation mechanism

The phase transformation mechanism combines thermodynamic driving forces with kinetic pathways uniquely enabled by our high oxygen vacancy concentration (25.6 %). From a thermodynamic perspective, the transition to monoclinic ZrO_2 can be expressed as contributions of different energies to the total energy:

$$\Delta G_{t\rightarrow m} = \Delta G_c + \Delta U_{se} + \Delta U_s$$

where $\Delta G_{t\rightarrow m}$ represents the total energy difference for transformation to monoclinic phase, ΔG_c is the chemical free energy difference, ΔU_{se} is the strain energy difference, and ΔUs is the interface energy difference [82].

oxygen vacancies fundamentally alter the energy landscape by introducing significant lattice strain [106]. Each vacancy creates a local distortion field that propagates through the surrounding lattice, with the cumulative effect of 25.6 % vacancies generating strain energy (ΔU_{se}) sufficient to reduce the crystallization barrier from > 1100°C to room temperature [106,107]. The transformation to monoclinic phase occurs when the total free energy change $\Delta G_{t\rightarrow m} = \Delta G_c + \Delta U_{se} + \Delta U_s$ becomes negative [82], where the vacancy-induced strain energy compensates for the unfavorable chemical free energy difference at room temperature.

The kinetic pathway, illustrated in Fig. 2(e), proceeds through a photon-assisted mechanism: (1) 405–532 nm photons are absorbed by electrons in vacancy-induced sub-bandgap states, with absorption efficiency proportional to vacancy concentration [81–83]; (2) photo-excited electrons are promoted to the conduction band, leaving behind positively charged vacancy sites; (3) atmospheric O_2 molecules act as electron scavengers, becoming activated O_2^- species [82,83]; (4) these activated oxygen species adsorb at surface vacancy sites, creating local charge imbalances that trigger Zr-O bond rearrangement [84]; (5) the ionic mobility enhancement from both vacancies and photo-excitation propagates the crystallization front through the material via a nucleation-growth mechanism [59,82,87].

This process fundamentally differs from thermal crystallization, where high temperatures provide the energy for atomic rearrangement but also promote vacancy annihilation through diffusion [89]. Our laser-induced mechanism operates at temperatures below the vacancy diffusion threshold, preserving the engineered defect structure within the final monoclinic phase.

4. Conclusions

This study presents a modified sol-gel synthesis method for producing amorphous ZrO_2 nanoparticles with enhanced oxygen vacancy concentrations. The method employs $Zr(OBu)_4$ as a precursor and acetylacetone (acac) as a chelating agent to control hydrolysis kinetics and facilitate oxygen vacancy formation through an 8-month aging process.

We characterized the oxygen deficient ZrO_2 using multiple complementary techniques including XPS, EPR, UV–vis spectroscopy, and Raman spectroscopy. XPS analysis indicates oxygen vacancy concentrations of approximately 25.6 % in the aged red-ZrO_2 compared to 9.2 % in conventional white-ZrO_2. The enhanced visible light absorption (340–600 nm) observed in UV–vis spectroscopy correlates with the presence of these oxygen vacancies and associated Zr^{3+} sites.

We characterize the chemical structure of the chelated precursor by FTIR spectroscopy and propose a symmetrical trimer model, which agrees with previous reports. We also investigate the laser-induced crystallization of the amorphous ZrO_2 nanoparticles by transient Raman micro-spectroscopy and observe rapid and irreversibly crystallization in the first seconds of irradiation. We attribute this phenomenon to the reactivity of oxygen vacancies with molecular oxygen present in the surrounding ambient atmosphere. We also propose a schematic mechanism for the crystallization process. XRD, TEM and SAED reveal that the laser-induced crystallization results in a polycrystalline monoclinic ZrO_2 arrangement. For comparison, thermally-induced crystallization of standard (white) and oxygen vacancy-rich amorphous ZrO_2 at 1170 °C is performed. It also leads to monoclinic ZrO_2, but with different colors (white and black), as expected.

The 8-month aging period, while necessary to achieve the exceptional 25.6 % oxygen vacancy concentration demonstrated here, represents a significant barrier to scalability. Future optimization strategies should explore: (i) controlled temperature aging (40–60°C) to accelerate peroxo complex formation without compromising vacancy generation, (ii) alternative chelating agents such as β-diketonates with enhanced complexation kinetics, (iii) ultrasonic or microwave-assisted processing to promote sol-gel reactions, and (iv) systematic optimization of the hydrolysis (r_w) and complexation (r_c) ratios to balance reaction speed with defect concentration.

We have successfully demonstrated both 2D patterning and 3D additive manufacturing of crystalline ZrO_2 structures, achieving millimeter-scale components through layer-by-layer processing. The fabrication of hollow squares and cylinders up to 3 mm in height validates the feasibility of this vacancy-mediated approach for producing complex ceramic architectures without high-temperature sintering. This room-temperature crystallization capability, enabled by our engineered oxygen vacancies, represents a paradigm shift from conventional ceramic processing and opens new possibilities for integrating functional ceramics with temperature-sensitive materials in next-generation devices.

CRediT authorship contribution statement

Fabrice Vaussenat: Writing – review & editing, Software. **Abbas Zirakjou:** Writing – original draft, Investigation. **Caroline A. Ross:** Writing – review & editing, Supervision, Funding acquisition. **Sylvain G. Cloutier:** Writing – review & editing, Supervision, Project

administration, Funding acquisition. **Benavides-Guerrero Jaime:** Writing – original draft, Visualization, Software, Investigation, Formal analysis, Data curation, Conceptualization. **Astrid C. Angel-Ospina:** Writing – original draft, Visualization, Supervision, Investigation, Formal analysis. **Luis F. Gerlein:** Visualization, Software, Methodology, Investigation, Data curation. **Abhiroop Bhattacharya:** Writing – review & editing, Validation, Methodology. **Paul Fourmont:** Writing – review & editing, Software, Methodology.

Declaration of Competing Interest

The authors declare that they have no known competing financial interests or personal relationships that could have appeared to influence the work reported in this paper.

Acknowledgements

S.G.C. acknowledges the NSERC-Discovery (Award: RGPIN-2022-03083) and Canada Research Chair Program (Award: CRC-2021-00490), CR acknowledges support from NSF (Award ECCS-2328839).

Appendix A. Supporting information

Supplementary data associated with this article can be found in the online version at doi:10.1016/j.addma.2025.104969.

Data availability

Data will be made available on request.

References

[1] D. Xu, et al., Microstructure and electrical properties of ZrO2-doped ZnO varistor ceramics, J. Mater. Sci. Mater. Electron 27 (2016) 767–771.
[2] S.S. Cheema, et al., Giant energy storage and power density negative capacitance superlattices, Nature 1–7 (2024), https://doi.org/10.1038/s41586-024-07365-5.
[3] A. Tabak, B. Safaei, A. Memarzadeh, S. Arman, C. Kizilors, An extensive review of piezoelectric Energy-Harvesting structures utilizing auxetic materials, J. Vib. Eng. Technol. 12 (2024) 3155–3192.
[4] U. Rathod, et al., Studies on ZrO2 nanoparticles for gas sensing application, Funct. Mater. Lett. 17 (2024) 2440002.
[5] T.K. Maiti, et al., Zirconia- and ceria-based electrolytes for fuel cell applications: critical advancements toward sustainable and clean energy production, Environ. Sci. Pollut. Res. 29 (2022) 64489–64512.
[6] F.F. Lange, Transformation toughening, J. Mater. Sci. 17 (1982) 225–234.
[7] Lange, F.F. J. Mater. Sci. 17, 235–239 (1982).
[8] S. Xiong, et al., Combination of plasma acoustic emission signal and laser-induced breakdown spectroscopy for accurate classification of steel, Anal. Chim. Acta 1336 (2025) 343496.
[9] Y. Zhou, Q. Zhang, X. Li, Y. Wang, Y. Guan, Mechanical performance of laser-textured metallic surface, J. Mater. Res. Technol. 33 (2024) 6084–6089.
[10] Z. Zhang, et al., Robotic wire-based friction stir additive manufacturing, Addit. Manuf. 88 (2024) 104261.
[11] K. Liu, et al., Binder jetting additive manufacturing of a 95W-3.5Ni-1.5Fe tungsten heavy alloy: enhanced ductility and dynamic deformation mechanisms, Mater. Sci. Eng. A 942 (2025) 148719.
[12] J. Long, et al., Printing dense and low-resistance copper microstructures via highly directional laser-induced forward transfer, Addit. Manuf. 103 (2025) 104755.
[13] Y. Zhao, et al., Dislocation motion in plastic deformation of nano polycrystalline metal materials: a phase field crystal method study, Adv. Compos. Hybrid. Mater. 5 (2022) 2546–2556.
[14] H. Yu, et al., The design of oxidation resistant ni superalloys for additive manufacturing, Addit. Manuf. 97 (2025) 104616.
[15] Y. Adraider, et al., Fabrication of titania coatings on stainless steel via laser-induced deposition of colloidal titanium oxide from sol–gel suspension, Mater. Chem. Phys. 138 (2013) 245–252.
[16] P.H. Bertrand, F. Bayle, C. Combe, P. Goeuriot, I. Smurov, Ceramic components manufacturing by selective laser sintering, Appl. Surf. Sci. 254 (2007) 989–992.
[17] J. Wilkes, Y. Hagedorn, W. Meiners, K. Wissenbach, Additive manufacturing of ZrO2-Al2O3 ceramic components by selective laser melting, Rapid Prototyp. J. 19 (2013) 51–57.
[18] Q. Wang, et al., Photocatalytic hydrogen generation on low-bandgap black zirconia (ZrO2) produced by high-pressure torsion, J. Mater. Chem. A 8 (2020) 3643–3650.
[19] Xu, Y. & Schoonen, M.A.A. The absolute energy positions of conduction and valence bands of selected semiconducting minerals. 85, 543–556 (2000).
[20] G. Pacchioni, Role of nanostructuring on the properties of oxide materials: the case of zirconia nanoparticles, Eur. J. Inorg. Chem. 2019 (2019) 751–761.
[21] Bui, T.S., Lovell, E.C., Daiyan, R. & Amal, R. Defective Metal Oxides: Lessons From CO2RR and Applications in NOxRR. Adv. Mater. n/a, 2205814.
[22] G.C. Vásquez, et al., Oxygen vacancy related distortions in rutile TiO2 nanoparticles: a combined experimental and theoretical study, Phys. Rev. B 94 (2016) 235209.
[23] B. Bharti, S. Kumar, H.-N. Lee, R. Kumar, Formation of oxygen vacancies and Ti^{3+} state in TiO_2 thin film and enhanced optical properties by air plasma treatment, srep32355, Sci. Rep. 6 (2016). srep32355.
[24] A. Sinhamahapatra, J.-P. Jeon, J. Kang, B. Han, J.-S. Yu, Oxygen-Deficient zirconia (ZrO2−x): a new material for solar light absorption, Sci. Rep. 6 (2016) 27218.
[25] F. Qi, Z. Yang, Y. Wang, Q. Qiu, H. Li, Defects in black zirconia responsible for solar energy harvesting, J. Mater. Chem. C. 9 (2021) 16732–16740.
[26] J. Ouyang, et al., The role of oxygen vacancies in phase transition and the optical absorption properties within nanocrystalline ZrO2, Nanomaterials 14 (2024) 967.
[27] S. Shukla, S. Seal, Mechanisms of room temperature metastable tetragonal phase stabilisation in zirconia, Int. Mater. Rev. 50 (2005) 45–64.
[28] J.R. Kelly, I. Denry, Stabilized zirconia as a structural ceramic: an overview, Dent. Mater. 24 (2008) 289–298.
[29] J. Chevalier, L. Gremillard, A.V. Virkar, D.R. Clarke, The Tetragonal-Monoclinic transformation in zirconia: lessons learned and future trends, J. Am. Ceram. Soc. 92 (2009) 1901–1920.
[30] E.H. Penilla, et al., Ultrafast laser welding of ceramics, Science 365 (2019) 803–808.
[31] L.F. Gerlein, J.A. Benavides-Guerrero, S.G. Cloutier, Laser-Assisted, Large-Area selective crystallization and patterning of titanium dioxide polymorphs, Adv. Eng. Mater. 22 (2020) 1901014.
[32] J. Wilkes, Y. Hagedorn, W. Meiners, K. Wissenbach, Additive manufacturing of ZrO2-Al2O3 ceramic components by selective laser melting, Rapid Prototyp. J. 19 (2013) 51–57.
[33] Z. Chen, et al., 3D printing of ceramics: a review, J. Eur. Ceram. Soc. 39 (2019) 661–687.
[34] M.H. Bocanegra-Bernal, S.D. de la Torre, Phase transitions in zirconium dioxide and related materials for high performance engineering ceramics, J. Mater. Sci. 37 (2002) 4947–4971.
[35] E.V. Frolova, M.I. Ivanovskaya, The origin of defects formation in nanosized zirconia, Mater. Sci. Eng. C. 26 (2006) 1106–1110.
[36] E. Zapata-Solvas, et al., Experimental synthesis and density functional theory investigation of radiation tolerance of Zr3(Al1-xSix)C2 MAX phases, J. Am. Ceram. Soc. 100 (2017) 1377–1387.
[37] J. Jiang, W. Ding, W. Zhang, H. Li, Defect-rich ZrO2 anchored pd nanoparticles for selective hydrodeoxygenation of bio-models at room temperature, Fuel 318 (2022) 123529.
[38] X. Jiao, et al., Engineering oxygen-deficient ZrO2-x nanoplatform as therapy-activated "immunogenic cell death (ICD)" inducer to synergize photothermal-augmented sonodynamic tumor elimination in NIR-II biological window, Biomaterials 272 (2021) 120787.
[39] M.S. G, P.S. Adarakatti, V. Udayakumar, Engineering of CuO/ZrO2 nanocomposite-based electrochemical sensor for the selective detection of hydrogen peroxide, Ionics 27 (2021) 5309–5322.
[40] S. Kumar, N. Gupta, B.D. Malhotra, Ultrasensitive biosensing platform based on yttria doped zirconia-reduced graphene oxide nanocomposite for detection of salivary oral cancer biomarker, Bioelectrochemistry 140 (2021) 107799.
[41] A. Sinhamahapatra, J.-P. Jeon, J. Kang, B. Han, J.-S. Yu, Oxygen-Deficient zirconia (ZrO2−x): a new material for solar light absorption, Sci. Rep. 6 (2016) 27218.
[42] M.A. Rahman, S. Rout, J.P. Thomas, D. McGillivray, K.T. Leung, Defect-Rich Dopant-Free ZrO_2 nanostructures with superior dilute ferromagnetic semiconductor properties, J. Am. Chem. Soc. 138 (2016) 11896–11906.
[43] F.K. McTAGGART, Reduction of zirconium and hafnium oxides, Nature 191 (1961) 1192.
[44] K.-O. Axelsson, K.-E. Keck, B. Kasemo, Surface compositional changes of ZrO2 in H2O, H2 and atomic hydrogen, investigated by aes and eels, Appl. Surf. Sci. 25 (1986) 217–230.
[45] C. Morant, J.M. Sanz, L. Galán, Ar-ion bombardment effects on ZrO2 surfaces, Phys. Rev. B 45 (1992) 1391–1398.
[46] D. Zu, et al., Black ZrO2 synthesized by molten lithium reduction strategy for photocatalytic hydrogen generation, J. Am. Ceram. Soc. 103 (2020) 4035–4042.
[47] J. Livage, Les procédés sol-gel: de l'art du feu à la chimie douce, Actual. Chim. Paris 1973 4–10 (1997).
[48] J. Livage, Chimie douce: from shake-and-bake processing to wet chemistry, N. J. Chem. 25 (2001) 1.
[49] R. Ciriminna, M. Pagliaro, G. Palmisano, Sol–Gel for environmentally Green products. in: The Sol-Gel Handbook, John Wiley & Sons, Ltd, 2015, pp. 1055–1070, https://doi.org/10.1002/9783527670819.ch34.
[50] E. Danks, A.R. Hall, S, Z. Schnepp, The evolution of 'sol–gel' chemistry as a technique for materials synthesis, Mater. Horiz. 3 (2016) 91–112.
[51] C. Gionco, et al., Cerium doped zirconium dioxide as a potential new photocatalytic material. The role of the preparation method on the properties of the material, Appl. Catal. Gen. 504 (2015) 338–343.

[52] Hidalgo Navío, G. Colón, S.G. Botta, M.I. Litter, Preparation and physicochemical properties of ZrO2 and Fe/ZrO2 prepared by a Sol−Gel technique, Langmuir 17 (2001) 202–210.
[53] M. Imran, et al., In-vitro hemolytic activity and free radical scavenging by sol-gel synthesized Fe3O4 stabilized ZrO2 nanoparticles, Arab. J. Chem. 13 (2020) 7598–7608.
[54] C. Imparato, et al., Unraveling the charge state of oxygen vacancies in ZrO2–x on the basis of synergistic computational and experimental evidence, J. Phys. Chem. C. 123 (2019) 11581–11590.
[55] J.A. Benavides-Guerrero, et al., Synthesis of vacancy-rich titania particles suitable for the additive manufacturing of ceramics, Sci. Rep. 12 (2022) 15441.
[56] M. Henry, J.P. Jolivet, J. Livage, Aqueous chemistry of metal cations: hydrolysis, condensation and complexation, in: R. Reisfeld, C.K. JJørgensen (Eds.), in: Chemistry, Spectroscopy and Applications of Sol-Gel Glasses, Springer, Berlin, Heidelberg, 1992, pp. 153–206, https://doi.org/10.1007/BFb0036968.
[57] A.C. Pierre, The chemistry of precursors solutions. in: Introduction to Sol-Gel Processing, Springer, Boston, MA, 1998, pp. 11–89, https://doi.org/10.1007/978-1-4615-5659-6_2.
[58] A.C. Pierre, The chemistry of precursors solutions BT, in: A.C. Pierre (Ed.), Introduction to Sol-Gel Processing, Springer US, Boston, MA, 1998, pp. 11–89, https://doi.org/10.1007/978-1-4615-5659-6_2.
[59] J.A. Benavides-Guerrero, et al., Synthesis of vacancy-rich titania particles suitable for the additive manufacturing of ceramics, Sci. Rep. 12 (2022) 15441.
[60] D. Hoebbel, T. Reinert, H. Schmidt, E. Arpac, On the hydrolytic stability of organic ligands in Al-, Ti- and Zr-Alkoxide complexes, J. Sol. Gel Sci. Technol. 10 (1997) 115–126.
[61] D.D. Agarwal, R. Jain, R.P. Bhatnagar, S. Srivastava, Synthesis and characterization of some peroxo complexes of zirconium, Polyhedron 9 (1990) 1405–1409.
[62] I. Georgieva, N. Danchova, S. Gutzov, N. Trendafilova, DFT modeling, UV-Vis and IR spectroscopic study of acetylacetone-modified zirconia sol-gel materials, J. Mol. Model 18 (2012) 2409–2422.
[63] W. Du, et al., Photocatalytic studies of Ho–Zr–O nano-composite with controllable composition and defects, Mater. Charact. 83 (2013) 178–186.
[64] T. Gyulavári, G. Veréb, Z. Pap, A. Dombi, K. Hernádi, Associating low crystallinity with peroxo groups for enhanced visible light active photocatalysts, Catal. Today 313 (2018) 231–238.
[65] R. Madhusudhana, M.A. Sangamesha, R.G.K. Urs, L. Krishnamurthy, G.L. Shekar, Synthesis and characterization of zirconia (ZrO2) by simple sol-gel route, Int. J. Adv. Res. 2 (2014) 433–436.
[66] H.S. Lim, A. Ahmad, H. Hamzah, Synthesis of zirconium oxide nanoparticle by sol-gel technique, AIP Conf. Proc. 1571 (2013) 812–816.
[67] K. Nakamoto, J. Fujita, S. Tanaka, M. Kobayashi, Infrared spectra of metallic complexes. Iv. comparison of the infrared spectra of unidentate and bidentate metallic complexes, J. Am. Chem. Soc. 79 (1957) 4904–4908.
[68] M. Chatry, M. Henry, M. In, C. Sanchez, J. Livage, The role of complexing ligands in the formation of non-aggregated nanoparticles of zirconia, J. Sol. Gel Sci. Technol. 1 (1994) 233–240.
[69] Socrates, G. Infrared and Raman Characteristic Group Frequencies: Tables and Charts, John Wiley & Sons, 2004).
[70] D. Peter, T.S. Ertel, H. Bertagnolli, EXAFS study of zirconium alkoxides as precursors in the sol-gel process: II. The influence of the chemical modification, J. Sol. Gel Sci. Technol. 5 (1995) 5–14.
[71] P.A. Connor, K.D. Dobson, A.J. McQuillan, New Sol-Gel attenuated total reflection infrared spectroscopic method for analysis of adsorption at metal oxide surfaces in aqueous solutions. Chelation of TiO2, ZrO2, and Al2O3 surfaces by catechol, 8-Quinolinol, and acetylacetone, Langmuir 11 (1995) 4193–4195.
[72] S.A. Dickie, A.J. McQuillan, In-Situ infrared spectroscopic studies of adsorption processes on boehmite particle films: exchange of surface hydroxyl groups observed upon chelation by acetylacetone, Langmuir 20 (2004) 11630–11636.
[73] J.V. Silverton, J.L. Hoard, Stereochemistry of discrete Eight-Coördination. II. The crystal and molecular structure of Zirconium(IV) acetylacetonate, Inorg. Chem. 2 (1963) 243–249.
[74] M.I. Osendi, J.S. Moya, C.J. Serna, J. Soria, Metastability of tetragonal zirconia powders, J. Am. Ceram. Soc. 68 (1985) 135–139.
[75] S. Jana, P.K. Biswas, Characterization of oxygen deficiency and trivalent zirconium in sol-gel derived zirconia films, Mater. Lett. 30 (1997) 53–58.
[76] D.L. Griscom, Amorphous materials: electron spin resonance, in: K.H.J. Buschow, et al. (Eds.), in: Encyclopedia of Materials: Science and Technology, Elsevier, Oxford, 2001, pp. 179–185, https://doi.org/10.1016/B0-08-043152-6/00038-3.
[77] M. Anpo, et al., Generation of superoxide ions at oxide surfaces, Top. Catal. 8 (1999) 189–198.
[78] Claudio Morterra, Elio Giamello, Luciana Orio, Marco Volante, Formation and reactivity of zirconium(3+) centers at the surface of vacuum-activated monoclinic zirconia, J. Phys. Chem. 94 (1990) 3111–3116.
[79] A. Punnoose, M.S. Seehra, ESR observation of W5+ and Zr3+ states in Pt/WOx/ZrO2 catalysts, Catal. Lett. 78 (2002) 157–160.
[80] A.B. Muñoz-García, et al., Origin and electronic features of reactive oxygen species at hybrid Zirconia-Acetylacetonate interfaces, ACS Appl. Mater. Interfaces 7 (2015) 21662–21667.
[81] T. Ghrib, et al., Structural, optical and radiation shielding properties of Zirconium–Titanium–Thallium ternary oxide (0.5ZrO2-(0.5-x)TiO2-xTl2O3), Ceram. Int. 47 (2021) 21837–21847.
[82] L. Liu, et al., From modification to mechanism: supercritical hydrothermal synthesis of nano-zirconia, Ceram. Int. 48 (2022) 4401–4423.
[83] K. Komaguchi, et al., Electron-Transfer reaction of oxygen species on TiO2 nanoparticles induced by Sub-band-gap illumination, J. Phys. Chem. C 114 (2010) 1240–1245.
[84] F. Sannino, et al., Oxidative degradation of phenanthrene in the absence of light irradiatiion by hybrid ZrO2-acetylacetonate gel-derived catalyst, Appl. Catal. B Environ. 156–157 (2014) 101–107.
[85] C. Ciszak, et al., Raman spectra analysis of ZrO2 thermally grown on zircaloy substrates irradiated with heavy ion: effects of oxygen isotopic substitution, J. Raman Spectrosc. 50 (2019) 425–435.
[86] B.-K. Kim, H. Hamaguchi, Mode assignments of the Raman spectrum of monoclinic zirconia by isotopic exchange technique, Phys. Status Solidi B 203 (1997) 557–563.
[87] J.A. Benavides-Guerrero, C.P. Trudeau, L.F. Gerlein, S.G. Cloutier, Laser selective photoactivation of amorphous TiO2 films to anatase and/or rutile crystalline phases, ACS Appl. Energy Mater. 1 (2018) 3607–3613.
[88] J. Manara, M. Arduini-Schuster, H.-J. Rätzer-Scheibe, U. Schulz, Infrared-optical properties and heat transfer coefficients of semitransparent thermal barrier coatings, Surf. Coat. Technol. 203 (2009) 1059–1068.
[89] X. Xin, T. Xu, J. Yin, L. Wang, C. Wang, Management on the location and concentration of Ti3+ in anatase TiO2 for defects-induced visible-light photocatalysis, Appl. Catal. B Environ. 176–177 (2015) 354–362.
[90] S. Limbu, Investigation of crystal structure confinement and optical attributes of monoclinic–tetragonal zirconia nanocrystals via chemical co-precipitation technique, Bull. Mater. Sci. 45 (2022) 182.
[91] J.A. Benavides-Guerrero, et al., Black anatase-TiO2 electrodes for sun-activated photocatalytic degradation of organic water contaminants, Surf. Interfaces 58 (2025) 105849.
[92] L. Puust, V. Kiisk, K. Utt, H. Mändar, I. Sildos, Afterglow and thermoluminescence of ZrO2 nanopowders, Cent. Eur. J. Phys. 12 (2014) 415–420.
[93] C. Carlone, Raman spectrum of zirconia-hafnia mixed crystals, Phys. Rev. B 45 (1992) 2079–2084.
[94] P. Ji, et al., Direct observation of enhanced Raman scattering on Nano-Sized ZrO2 substrate: charge-transfer contribution, Front. Chem. 7 (2019).
[95] M. Sternik, K. Parlinski, Lattice vibrations in cubic, tetragonal, and monoclinic phases of ZrO2, J. Chem. Phys. 122 (2005) 064707.
[96] H. Qin, W. Guo, J. Liu, H. Xiao, Size-controlled synthesis of spherical ZrO2 nanoparticles by reverse micelles-mediated sol-gel process, J. Eur. Ceram. Soc. 39 (2019) 3821–3829.
[97] P. Chelliah, et al., Photocatalytic organic contaminant degradation of Green synthesized ZrO2 NPs and their antibacterial activities, Separations 10 (2023) 156.
[98] Y. Wang, X. Liu, S. Pan, Q. Zhou, J. Shu, Local structure regulation and spectroscopy study of blue cubic zirconia, CrystEngComm 25 (2023) 1582–1588.
[99] C. Mita, et al., High stability and photocatalytic activity of N-doped ZrO2 thin films, J. Alloy. Compd. 1002 (2024) 175134.
[100] S.N. Basahel, T.T. Ali, M. Mokhtar, K. Narasimharao, Influence of crystal structure of nanosized ZrO2 on photocatalytic degradation of methyl Orange, Nanoscale Res. Lett. 10 (2015) 73.
[101] NIST X-ray Photoelectron Spectroscopy Database. ⟨https://srdata.nist.gov/xps/SpectralByCompdDd/2845⟩.
[102] P. Lackner, Z. Zou, S. Mayr, U. Diebold, M. Schmid, Using photoelectron spectroscopy to observe oxygen spillover to zirconia, Phys. Chem. Chem. Phys. 21 (2019) 17613–17620.
[103] S. Song, et al., Oxygen vacancies generated by Sn-doped ZrO 2 promoting the synthesis of dimethyl carbonate from methanol and CO 2, RSC Adv. 11 (2021) 35361–35374.
[104] C. Gionco, et al., Paramagnetic defects in polycrystalline zirconia: an EPR and DFT study, Chem. Mater. 25 (2013) 2243–2253.
[105] M.F. Bekheet, et al., A quantitative microscopic view on the gas-phase-dependent phase transformation from tetragonal to monoclinic ZrO2, J. Am. Ceram. Soc. 107 (2024) 5036–5050.
[106] D.S. Aidhy, K. Rawat, Coupling between interfacial strain and oxygen vacancies at complex-oxides interfaces, J. Appl. Phys. 129 (2021) 171102.
[107] D.Z. Gao, J. Strand, M.S. Munde, A.L. Shluger, Mechanisms of oxygen vacancy aggregation in SiO2 and HfO2, Front. Phys. 7 (2019).